

An ultrafast pulse-dilation framing camera and its application for time-resolved X-ray diagnostic *

Houzhi Cai,¹ Qiuyan Luo,¹ Kaixuan Lin,¹ Xuan Deng,¹ Junkai Liu,¹ Kaizhi Yang,¹ Dong Wang,¹ Jiajie Chen,¹ Jiaheng Wang,¹ Jinghua Long,¹ Lihong Niu,¹ Yunfei Lei^{1,†} and Jinyuan Liu^{1,†}

¹*Key Laboratory of Optoelectronic Devices and Systems of Ministry of Education and Guangdong Province, College of Physics and Optoelectronic Engineering, Shenzhen University, Shenzhen 518060, China*

An ultrafast framing camera with a pulse-dilation device and a microchannel plate (MCP) imager as well as an electronic imaging system is reported. The camera achieves a temporal resolution of 10 ps by using a pulse-dilation device and a gated MCP imager, and a spatial resolution of 100 μm by using an electronic imaging system composed of combined magnetic lenses. The spatial resolution characteristics of the camera are theoretically and experimentally studied. The results show that the camera with combined magnetic lenses could reduce field curvature and acquire a larger working area. A working area 53 mm in diameter has been achieved by applying four magnetic lenses to the camera. Furthermore, the camera is used to detect X-rays produced from a laser targeting device. The diagnostic results show that the width of the X-ray pulse is about 18 ps.

Keywords: Inertial confinement fusion, Plasma diagnostics, Framing camera, Combined lenses, Pulse-dilation.

I. INTRODUCTION

X-ray framing camera based on gated microchannel plate (MCP) is an essential diagnostic instrument in the inertial confinement fusion (ICF) study, the Z-pinch experiment, laser plasma physics, and so on [1–8]. Such cameras use a microstrip transmission line photocathode (PC) deposited on the MCP surface to transmit a short gating pulse [9,10], and the temporal sampling for the signal is obtained while the signal is synchronized with the gating pulse [11,12]. The temporal resolution of such a camera is limited by the transit time spread of electrons traversing the MCP channel pore [13–15]. While the camera consists an MCP 0.5 mm thick, the temporal resolution range is from 60 to 100 ps. In ICF experiments, the temporal resolution of such a camera does not meet the requirement for acquiring the detailed history of implosion with 100–200 ps duration [16–18]. A faster camera should be used for the accurate characterizing of the implosion performance [19,20]. Lately, a dilation X-ray imager (DIXI) with pulse-dilation technology was developed by Hilsabeck et al. [21]. The temporal resolution of such imager is better than 10 ps [21–25]. The temporal width of the electron beam generated by the PC was dilated up to 50 times in the 50 cm drift region to achieve a high temporal resolution. Because the transmission distance of electron beam in drift region is too long, an electronic optical system should be employed for imaging the electron beam from PC onto MCP to achieve a high spatial resolution. In the DIXI, four magnet coils were

employed to achieve a spatial resolution of 510 μm for the Au PC [21,22]. The single-line-of-sight (SLOS) camera developed by Nagel et al. used a Cu winding outside of the evacuated drift tube to produce a magnetic field. A spatial resolution of 35 μm and working area with 25.6 mm \times 12.8 mm were achieved [26,27]. Another 4 ps dilation framing camera used a short magnetic lens to image the electrons, and a spatial resolution of about 100 μm with the magnification ratio of 1:1 was obtained [28]. However, the variations of the spatial resolution within the working area have not been reported in the dilation framing camera with short magnetic lens. Generally, the off-axis spatial resolution will be reduced due to the field curvature of the camera electronic optical imaging system using short magnetic lens, which limits the working area as well as the spatial resolution of the camera. Here, combined magnetic lenses are used in our framing camera to correct the field curvature. Such a magnetic lens is frequently used to observe an electron moiré pattern or achieve a high imaging quality in the electron microscopes and streak cameras [29–32].

In this paper, an ultrafast framing camera with pulse-dilation technology and combined magnetic lenses is presented, and an X-ray diagnosis experiment is described. In the camera, four magnetic lenses are combined to reduce the field curvature, and a spatial magnification ratio of 1:1 is designed. The temporal resolution measurement of camera is performed by a femtosecond laser and a fiber bunch. The electronic optical imaging characteristics of the camera, such as the spatial resolution, the field curvature and the sensitive area are also performed. Furthermore, the camera is used to detect X-rays, which is produced from a terawatt laser targeting system.

II. CAMERA PARAMETERS

* Supported by the Program for National Natural Science Foundation of China (NSFC) (11775147); Guangdong Basic and Applied Basic Research Foundation (2019A1515110130); Shenzhen Science and Technology Program (Nos. JCYJ20210324095007020 and JCYJ20200109105201936)

† Corresponding authors, leiyunfly@163.com and ljjy@szu.edu.cn

The ultrafast pulse-dilation framing camera is made up of a pulse-dilation device, an MCP imager, a combined lenses imaging system, and a pulse generator, its schematic diagram and photograph are respectively shown in Figs. 1(a) and (b). The pulse-dilation device includes three microstrip X-ray PCs, an anode mesh, and a drift tube. The PCs are developed by coating an Au film with thickness of 80 nm onto a $(C_8H_8)_n$ film. The width for each PC is 12 mm, and the gap between two neighbouring PCs is 10 mm. The PC has two functions, one is used to convert the X-rays into electrons, and the other is used as a microstrip transmission line to transmit the dilation electric pulse. The anode mesh is mounted 1.8 mm from PC and connected to ground. Each PC strip is applied with a high direct current (DC) voltage overlaying the dilation pulse, which gives a varying PC voltage. The energy of the electron arriving at mesh is provided by the varying PC voltage. An electron emitted from the PC earlier has a larger energy and a higher speed than those emitted later. Hence, electron energy spread is obtained, resulting in the temporal magnification of the electron pulse in the 550 mm drift tube.

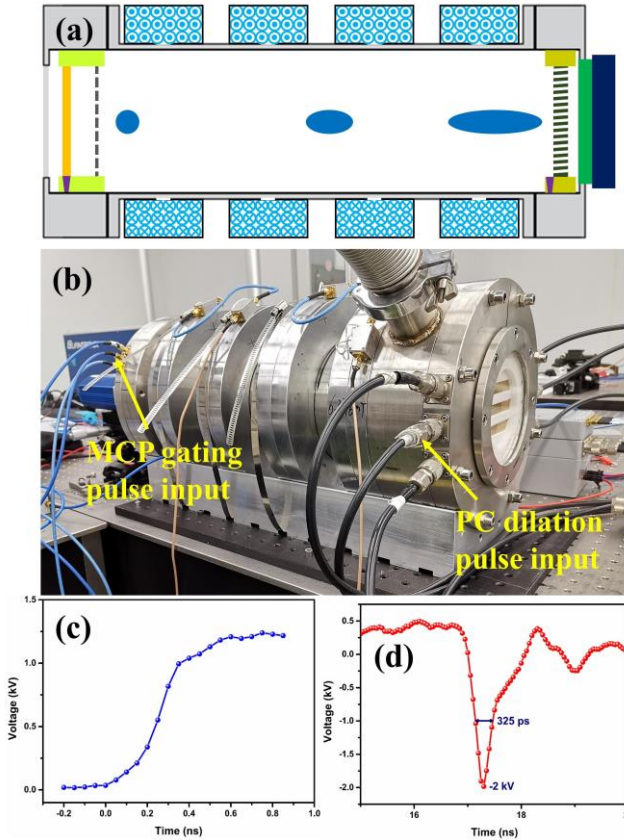


Fig. 1. (a) The schematic diagram of the ultrafast pulse-dilation framing camera. (b) The photograph of the camera. (c) The rising edge waveform of the PC dilation pulse with an effective rising time of about 400 ps and a slope of about 2.5 V/ps. (d) The waveform of the MCP gating pulse with an amplitude of -2 kV and a width of 325 ps.

The MCP imager is composed of a MCP, a phosphor screen, and a CCD. The MCP has a thickness of 0.5 mm, a diameter of 106 mm, and a pore diameter of 12 μm . The three microstrip transmission lines are formed by depositing 500 nm

Cu overlaid by 100 nm of Au on the MCP input surface. The whole MCP output surface is also deposited by the Cu and Au with the same thicknesses, and is connected to ground. The width of 12 mm for each microstrip transmission line, and a 10 mm gap between two adjacent lines is formed. The phosphor screen is biased with a +3.4 kV DC voltage and positioned 0.5 mm from the MCP. A CCD is fibre coupled with the phosphor screen to capture the visible light images.

The drift region for the electron pulse-dilation is 550 mm from the mesh to the MCP. With the travelling in the drift tube, the electrons are imaged from PC to MCP by an axially symmetric nonuniform magnetic field, which is produced by the combined magnetic lenses [28,33]. Four identical annular magnetic lenses are used to form the combined lenses imaging system. The magnetic lens composed of a soft iron frame and a 2320-turn copper coils has an outer diameter of 256 mm, an inner diameter of 160 mm, and an axial length of 50 mm. In the inner cylinder, a 4 mm circular slit is formed for the releasing of the magnetic field from soft iron to drift tube.

The pulse generator outputs three PC dilation pulses and three MCP gating pulses. It consists of a transistor ramp pulser and a pulse width shortening diode circuit. In the transistor ramp pulser, eight avalanche transistors are stacked in a string, and seven strings are configured in a Marx bank circuit. The transistor ramp pulser produces six ramp pulses, with three of them used for PC dilation pulses to drive the three PCs, and the other three separately driving the diode circuit for producing the three MCP gating pulses [28]. Each PC dilation pulse has an effective rising time of about 400 ps, as shown in Fig. 1(c). The slope of the PC dilation pulse is about 2.5 V/ps. Furthermore, the MCP gating pulse is obtained with an amplitude of -2 kV and a width of 325 ps, whose waveform is shown in Fig. 1(d).

III. PERFORMANCE MEASUREMENT RESULTS

3.1 Spatial resolution measurement

The spatial resolution of camera as well as the temporal resolution are measured. To measure the spatial resolution with different off-axis distance, a tailored Au PC instead of the X-ray PC is used. The Au PCs are formed by depositing an 80 nm Au film onto a quartz substrate. A resolution mask is developed by using photolithography for each PC [34]. The resolution mask is made up of several slits, with 3 mm \times 3 mm squares for each slit. The spatial frequencies of the slits are various, which are 500, 200, 100, 66, 50, 40, 33 and 28 μm , respectively. Two slits with the directions of parallel and perpendicular to the PC transmission line are used for each spatial frequency. The eight spatial frequencies with sixteen slits are formed to a slit group. Several slit groups are deposited repetitively along each PC to measure the spatial resolution with different off-axis distance.

The spatial resolution of the camera is determined by the combined magnetic lenses and the MCP imager, it could be given by [19,22]:

$$\delta = \sqrt{(\delta_{\text{drift}})^2 + (\delta_{\text{MCP}} \times M_s)^2}. \quad (1)$$

Where δ_{drift} is the spatial resolution of the combined magnetic lenses, $\delta_{MCP} = 50 \mu\text{m}$ is the spatial resolution of the MCP imager, and the spatial magnification ratio M_s is 1. As δ_{MCP} and M_s are fixed, δ is mainly influenced by the combined magnetic lenses.

Simulations of the spatial resolution have been carried out. The Lorentz3DEM software is used to simulate the electromagnetic field from PC to MCP of the camera and the resulting electron trajectories are traced. The spatial resolution of each off-axis position is obtained by the Rayleigh criterion. At a certain position on PC, there are two photoelectron beams emitted, and their corresponding image points on MCP are obtained. The minimum distinguishable distance between the two image points is obtained by using the Rayleigh criterion, and the corresponding gap of the two photoelectron beams on PC is determined as the spatial resolution.

The static spatial resolution measurements are performed using a DC ultraviolet source. Both of the PC and MCP are applied with a static DC voltage. The PC converts the incident ultraviolet light to photoelectron image with mask. Then, the photoelectron image is imaged onto MCP by the combined magnetic lenses, and it is converted to a corresponding visible image by the MCP imager. Finally, a CCD is used to capture the visible image.

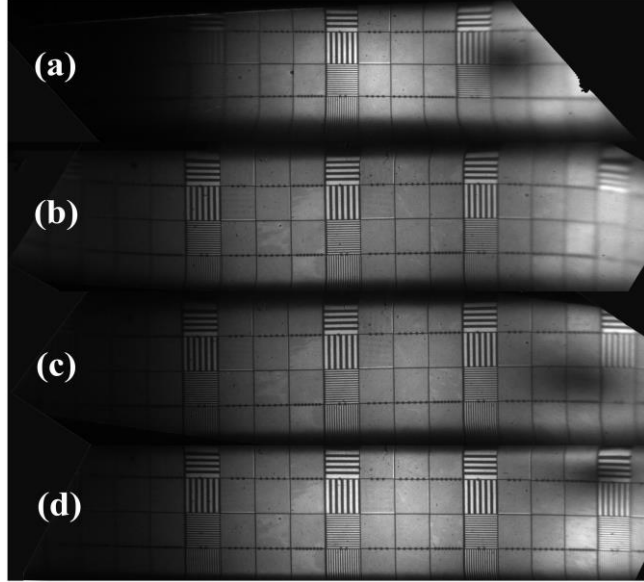


Fig. 2. (a) The static image with resolution mask on Gaussian plane of the middle PC, the camera has one magnetic lens. (b) The static image for the camera with two magnetic lenses. (c) The static image of the camera consisted of three magnetic lenses. (d) The static image while the camera uses four magnetic lenses.

The spatial resolution characteristics of the camera with different number of magnetic lenses are compared. The number of the magnetic lenses is increased in turn, and the static image of the corresponding camera is obtained, respectively. When the camera consists one magnetic lens, the static image on the Gaussian plane of the middle transmission PC is shown in Fig. 2(a). When the camera is with two, three, or four magnetic lenses, the static images

with resolution masks are shown in Figs. 2(b), (c), and (d), respectively. The spatial resolution is obtained from the static image, and the modulations of the slits for different spatial frequencies could be given by:

$$M = \frac{I_{\max} - I_{\min}}{I_{\max} + I_{\min}}. \quad (2)$$

Where I is the corresponding intensity of the slit image, I_{\max} is the maximum value of the intensity, and I_{\min} is the minimum intensity. The measurement results are compared with the simulation results.

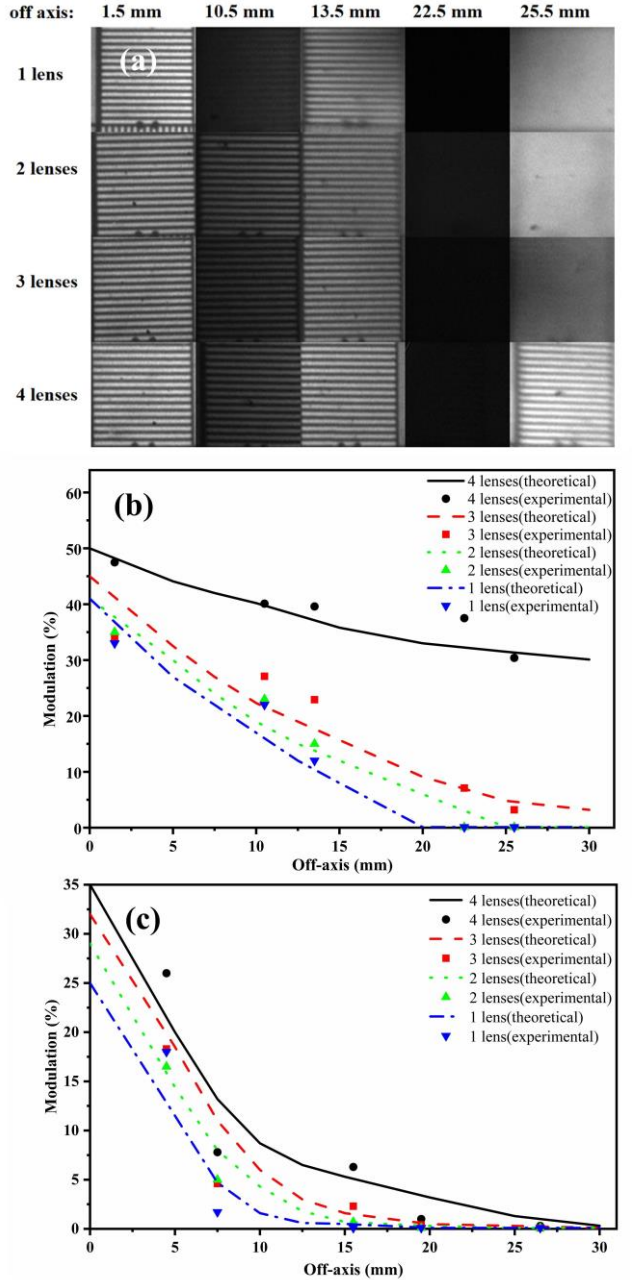


Fig. 3. (a) The 200 μm mask on Gaussian plane for different off-axis distance and various magnetic lens number. (b) The modulation of the 200 μm mask in (a) versus the off-axis distance. (c) The modulation of 100 μm mask on Gaussian plane various with off-axis distance.

The 200 μm mask for different off-axis distances and various magnetic lens numbers are shown in Fig. 3(a), and its corresponding modulations are shown in Fig. 3(b). The lines are the simulation results and the points represent the measurement results. The camera consisting of one magnetic lens has the worst imaging quality. The modulation decreases quickly with increasing off-axis distance. It cannot distinguish 200 μm when the off-axis distance is larger than 13.5 mm. The camera with two, three, or four magnetic lenses has much better imaging quality than the one magnetic lens camera. When the camera uses four magnetic lenses, its spatial resolution is better than that of two or three lenses. In the camera with four magnetic lenses, all of the effective working area with diameter of 60 mm can deliver a spatial resolution of better than 200 μm . The measurement results agree well with the simulated results, and show that the modulation is worse with the increasing off-axis distance. That is to say, the spatial resolution will be reduced while the off-axis distance is increased.

The modulations of the 100 μm masks on the Gaussian plane versus off-axis distances are shown in Fig. 3(c). It shows that the visibility of the 100 μm mask is reduced while the off-axis distance is increased. The 100 μm mask can be distinguished within the area with radius of 4.5 mm while using one magnetic lens. The imaging quality is improved significantly while the camera uses four magnetic lenses. However, the 100 μm mask in the PC off-axis 26.5 mm does not have visible modulation. The camera cannot have working area with radius of 26.5 mm for the 100 μm spatial resolution on the Gaussian plane. Furthermore, the modulation for the 100 μm descends faster than that of 200 μm along the off-axis distance.

The off-axis spatial resolution is mainly influenced by the field curvature. Field curvature is a type of aberration and makes the imaging plane to a curved imaging surface. The curvature close to the axis is approximately spherical. In the magnet lenses imaging system, the curvature radius r_p of the image surface is given by [35]:

$$\frac{1}{r_p} = -\frac{e}{4mV^4} \int_{-\infty}^{+\infty} B^2 dz. \quad (3)$$

Here, e and m are respectively the electron charge and mass, V is the voltage between PC and mesh, B is the magnetic field strength in the drift tube, and z is the axial direction variable.

Field curvature is a complex parameter because the curvature radius r_p varies with the off-axis distance. The imaging surface is simulated by using the Lorentz3DEM software. The curved imaging surfaces for the cameras with different number of lenses are shown in Fig. 4(a), and its two-dimension projections are show in Fig. 4(b). The lines are the simulation results with the simulation PC area diameter of 60 mm. The parameter L is the distance from the imaging surface to the PC along axis, which represents the position of the imaging surface for each off-axis point. The simulation results show that the imaging surface is a curved surface while the PC voltage is fixed. While the object point has larger off-axis distance, its corresponding L is smaller, which represents that

the position of the imaging point is closer to PC for the farther off-axis object point.

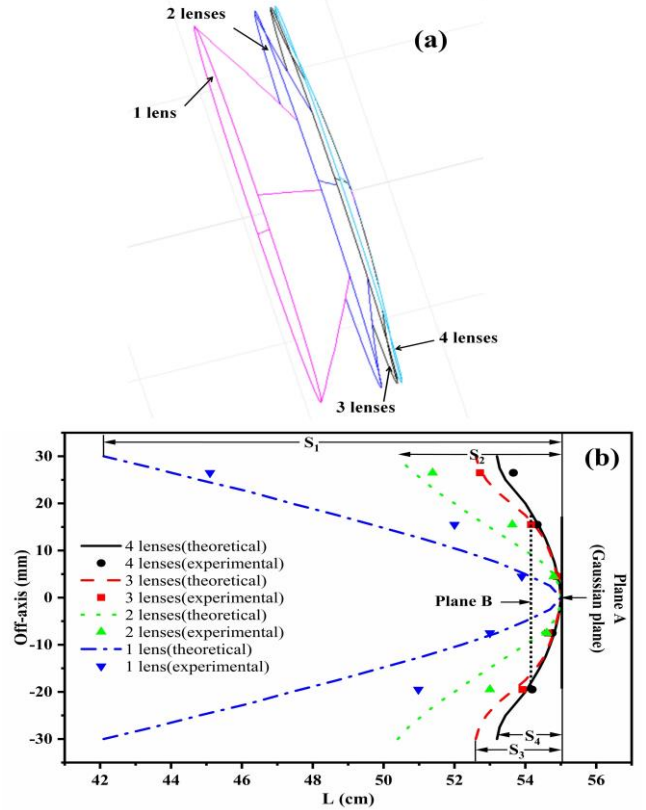


Fig. 4. (a) Simulation drawing of the field curvatures with different magnet lenses. (b) Two-dimension projections of the field curvature, plane A is the Gaussian plane, plane B is another imaging plane to achieve a larger PC sensitive area and reduce the spatial resolution differences in the working area.

In the experiment, the imaging surface is detected by a planar MCP, the distance between the PC and the MCP is fixed in the camera. Therefore, the position of the imaging point for each off-axis object point cannot be obtained simultaneously in an experiment with the same PC voltage. The imaging point positions are obtained in the different experiments with different PC voltages. The PC voltage is adjusted in turn, resulting in that the clearest area of the image on MCP is varied in sequence. Then, the PC voltage for each object point on PC imaged clearly on MCP can be obtained. In the camera with four magnetic lenses, it can be derived from the experimental results that the distance between the object plane and image surface will be reduced about 0.14 mm while the PC voltage is increased 1 V. Similar results can be obtained in the other magnetic lenses imaging systems. Therefore, the PC voltage variation can be used to obtain the variation of imaging surface position, and the imaging point position of each PC object point can be obtained [35]. The experimental results of the imaging point position versus the off-axis distance of the PC object point are shown in Fig. 4(b). In Fig. 4, the lines are the simulation results, and the points are the experimental results. The experimental results are consistent with the simulation results. The position of the

imaging point will be moved to PC while the off-axis distance of the object point is increased, which lead to a curved imaging surface. However, the detector of the curved imaging surface is a planar MCP, the electrons imaged onto the planar MCP, result in the spatial resolution varying with the off-axis distance of the electron emitted from PC. That is to say, the spatial resolution uniformity in whole PC sensitive area will be reduced.

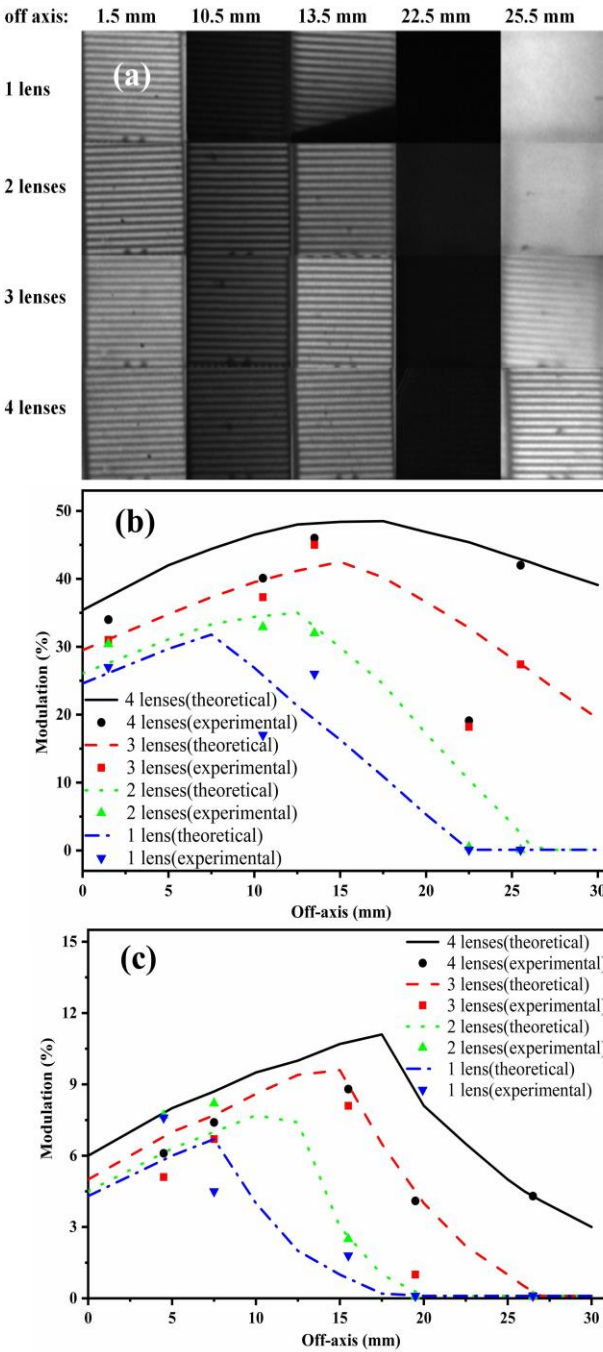


Fig. 5. (a) The static images of 200 μm masks on imaging plane B. (b) The modulations of 200 μm masks on imaging plane B various with the off-axis distance. (c) The modulations of the 100 μm masks on imaging plane B versus off-axis distance.

In Fig. 4(b), the plane A is the Gaussian plane, and the curved imaging surfaces are the Petzval surfaces [35]. S_1 , S_2 , S_3 , and S_4 are the axial deviations between the Gaussian plane and the Petzval surface with the aperture radius of 30 mm. It can be shown that the maximum in the camera with one magnetic lens, S_1 is about 13 cm. The deviation S_2 is decreased to 5 cm by using two magnetic lenses. Better curvature is achieved by using three magnetic lenses, and the deviation S_3 is about 2.5 cm. The field curvature has been further improved in the camera with four magnetic lenses, and the deviation S_4 is improved to less than 2 cm. The improvement of the field curvature brings improving spatial resolution with the increasing number of magnetic lenses, which can explain the experimental results in Fig. 3.

To improve the spatial resolution uniformity in whole PC sensitive area, the location of the Gaussian plane A for the camera imaging system is adjusted. The PC voltage of -3 kV is fixed, the magnetic lens excitation currents are reduced. Then, the Gaussian plane A is moved farther from the PC. While the plane B in Fig. 4(b) is moved to overlap with the MCP plane, the spatial resolution differences in the working area will be improved. Fig. 5(a) shows the 200 μm static images of the slits on the imaging plane B, and its modulations varying with off-axis distance are obtained, as shown in Fig. 5(b). Compared with the results of Gaussian plane A in Fig. 3(a), the spatial resolution of off-axis 25.5 mm is significantly improved. The 200 μm mask on the radius of 25.5 mm can be distinguished in the camera with four and three magnetic lenses. Fig. 5(b) shows the changing of the imaging plane from A to B brings the improvement of the modulation for the off-axis area. However, the modulation of the on-axis area will be decreased. Fortunately, the spatial resolution differences in the whole working area are improved. Comparing the modulation difference of plane B in Fig. 5(b) with that of plane A in Fig. 3(b), the modulation difference among the points within 30 mm off-axis distance in plane B is better than that in plane A. That is to say, the spatial resolution uniformity of the whole working area for plane B is better than that for plane A.

The modulations of the 100 μm slits for the static images on the imaging plane B are shown in Fig. 5(c). The 100 μm spatial resolution with radius of 26.5 mm can be distinguished in the camera with four magnetic lenses. It also can be shown that the combined multiple magnetic lenses have a better imaging quality than that of only one magnetic lens. The camera with four combined magnetic lenses can achieve a spatial resolution of 100 μm in a sensitive area of 53 mm in diameter.

3.2 Temporal resolution measurement

The energy spread at the mesh results in a temporal magnification of the electron pulse in the drift tube, which greatly improves the temporal resolution. The temporal resolution T of pulse-dilation framing camera is mainly determined by the temporal resolution T_{MCP} of the MCP imager and the pulse-dilation temporal magnification factor M , and it is given by [21]:

$$T \approx \frac{T_{MCP}}{M}, \quad (4)$$

The pulse-dilation temporal magnification factor M is decided by the PC voltage, the PC dilation pulse slope, and the drift tube length [26]. Because of the small distance from PC to mesh, as well as the negligible initial electron energy spread at PC, the electrons which get into the drift tube at time t_i will get to MCP at time as follows [25]:

$$t'_i = \frac{L_{pm}}{\sqrt{2e\phi(t_i)/m}} + t_i, \quad (5)$$

where L_{pm} is the 550 mm length of the drift tube. Between two-time steps, the temporal magnification factor M can be given as [33]:

$$\begin{aligned} M(t_{i+1}, t_i) &= \frac{t'_{i+1} - t'_i}{t_{i+1} - t_i} = 1 + \frac{L_{pm}}{\sqrt{2e/m}} \frac{\phi(t_{i+1})^{-1/2} - \phi(t_i)^{-1/2}}{t_{i+1} - t_i} \\ &\approx 1 + \frac{L_{pm}}{\sqrt{2e/m}} [\phi(t)^{-1/2}]. \end{aligned} \quad (6)$$

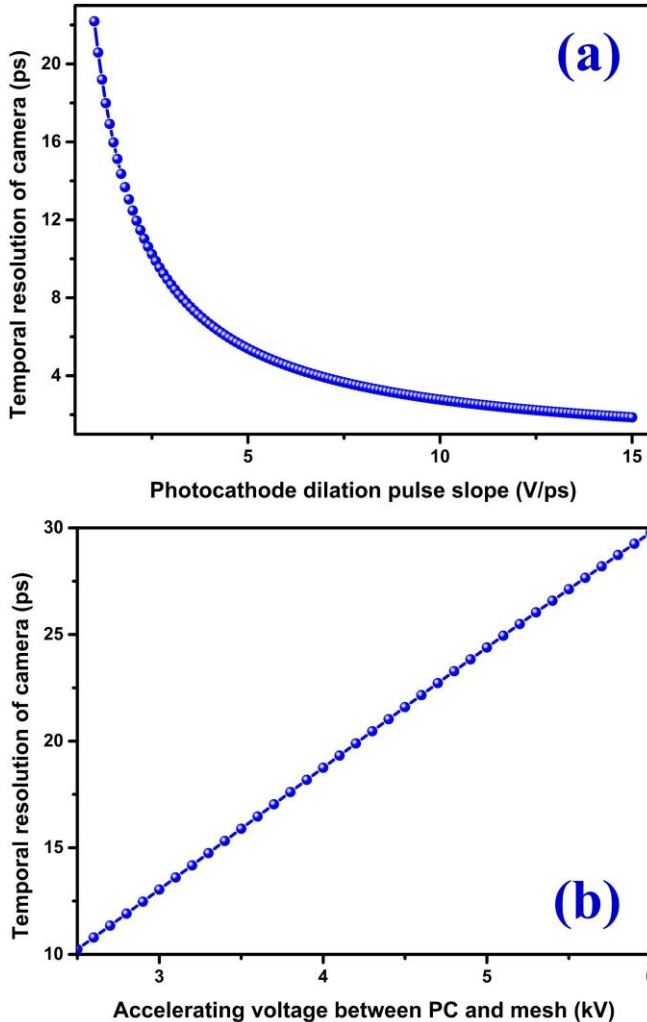


Fig. 6. (a) The temporal resolution of camera varying with the PC dilation pulse slope. (b) The temporal resolution of camera versus accelerating voltage.

Generally, the drift tube length is determined when the pulse-dilation framing tube is designed. Then, the temporal resolution T is mainly determined by the PC voltage, the PC dilation pulse slope, and the resolution of MCP imager [26]. While the temporal resolution of MCP imager is 100 ps, the temporal resolution T of camera varying with the PC dilation pulse slope, as well as its relationship with PC voltage are studied, as shown in Fig. 6. An improving temporal resolution will be achieved while the PC dilation pulse slope is increased. This is because that the temporal magnification factor M increases when the PC dilation pulse slope is increased. In Fig. 6(a), a voltage of -2.5 kV is applied to PC. In Fig. 6(b), the PC dilation pulse slope is 2.5 V/ps. Fig. 6(b) shows that the temporal resolution is improved with a decreasing accelerating voltage. The accelerating voltage is a very important parameter of the camera. Both of the electron transit time spread from PC to anode mesh and the spatial resolution improve with the increasing of acceleration voltage [31,32]. Generally, the acceleration voltages of the pulse-dilation framing cameras are higher than 2.5 kV [21,36].

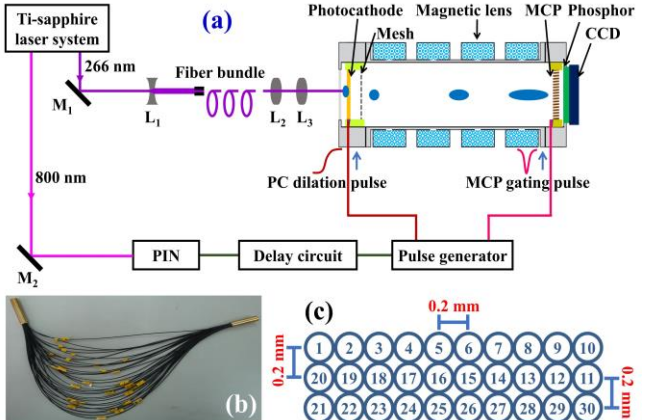


Fig. 7. (a) Schematic diagram of experimental setup for the temporal resolution measurement. (b) The photograph of the fiber bundle. (c) The output port array of the fiber bundle. The fiber labeled 1 is the shortest fiber. There is a 0.2 mm gap between each two centers of the neighbouring fibers.

The temporal resolution measurement is performed by a femtosecond laser and a fiber bundle. Its measurement setup includes Ti-sapphire femtosecond laser system, optical time adjustment system, fiber bundle, optical imaging system, electric trigger signal generator, electric delay circuit, and the pulse-dilation framing camera, as shown in Fig. 7(a). Two laser beams with wavelengths of 266 nm and 800 nm are exported from the femtosecond laser system. The 266 nm UV light is used to excite photoelectron, and the 800 nm infrared light is used as a synchronous trigger signal. The UV light with 130 fs in pulse width is reflected by a total reflection mirror M₁, and then the spot size of UV light is enlarged by a concave lens L₁. The fiber bundle composes of 30 fibers, and is used to separate the input UV laser into 30 light points. The lengths of the 30 fibers are increased with an equal difference of 2 mm, and the error is less than 0.2 mm. Therefore, the 30 UV light points are outputted at varying times. A delay time of about 10 ps is achieved for each two adjacent light points.

The photograph of the fiber bundle and the array diagram of the fiber output port are respectively shown in Fig. 7(b) and (c). The 30 UV light points exported from fiber bundle are imaged onto PC by using the lenses L_2 and L_3 , which generates 30 photoelectron pulses. The emitting time interval for each pair of neighbouring photoelectron pulses is about 10 ps.

First, the static image of the 30 laser pulses is measured, as shown in Fig. 8(a). The PC and MCP are respectively applied with a static DC voltage of -3 kV and -700 V. The top right image point is imaged from the shortest fiber, and there are 0.5 mm distance between every two neighbouring images. The static image represents the light intensity uniformity of the 30 light points, which is used as a normalized background image for the gating image.

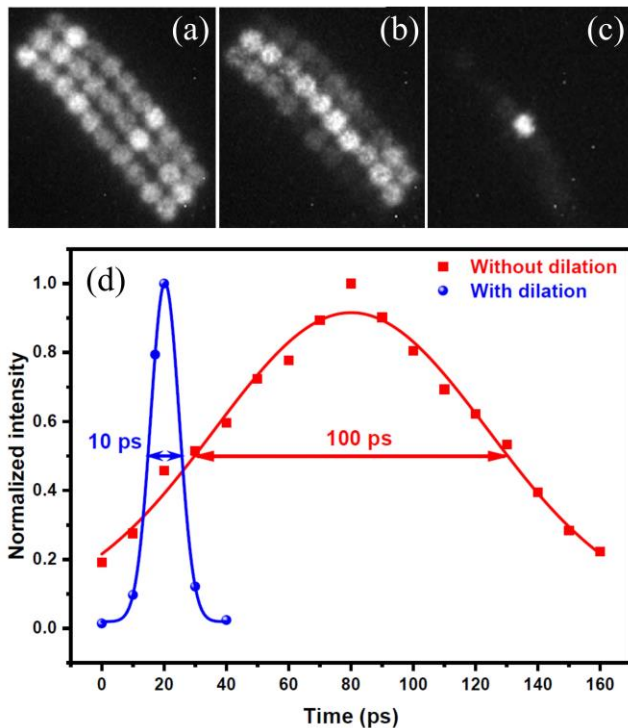


Fig. 8. (a) The static image of the 30 laser pulses, a static DC voltage of -3 kV is applied to PC and a -700 V is for MCP. (b) The gating image of the 30 laser pulses for the camera without pulse-dilation, only a -2.5 kV DC voltage is for PC, and a -483 V DC bias plus the gating pulse described above are applied on MCP. (c) The gating image of 30 laser pulses for the camera with pulse-dilation, a -3 kV DC bias overlying by the 2.5 V/ps PC dilation pulse are for PC, and a -483 V DC bias plus the gating pulse are applied on MCP. (d) The measured results of the temporal resolution, the red data are the results without pulse-dilation for (b), and the blue data are the results with pulse-dilation for (c).

Then, the gating image for the camera without pulse-dilation is measured, as shown in Fig. 8(b). It is obtained with a -2.5 kV static DC voltage applied on PC and a -483 V DC bias plus the gating pulse as described above for MCP. As a static DC bias is applied on PC, the electron beam is not temporal dilated. Whereas the MCP is driven by the gating pulse, and the electron signal will be sampled by the MCP imager. In short, this experiment measures the gate

width of the MCP imager. Figs. 8(a) and (b) are two raw CCD images. To reduce the affect caused by the nonuniform light intensity distribution, the static results from Fig. 8(a) are used to correct the gating results in Fig. 8(b). A lineout of the corrected data is shown in red in Fig. 8(d). The solid red block points are experimental results, and they are Gaussian fitted to obtain the intensity versus time curve. The FWHM of the Gaussian curve is defined as the temporal resolution of camera. Fig. 8(d) shows that, while the electron signal is not dilated, the temporal resolution is approximately 100 ps, which is the temporal resolution T_{MCP} of the MCP imager.

Finally, the gating image for the camera with pulse-dilation is measured, as shown in Fig. 8(c). The MCP is gated, applied with a -483 V DC bias and the gating pulse, the same as that for Fig. 8(b). The experimental parameters different from that for Fig. 8(b) is the PC voltage, which is that the PC is excited by a dilation pulse and a -3 kV DC bias. Therefore, the photoelectron pulses are temporally dilated, and the temporal resolution of camera will be improved significantly, as shown in equation (4). To obtain the pulse dilation, all or part of the 30 photoelectron pulses are synchronized with the rising edge of the PC dilation pulse. In this experiment, the arrival time of the laser pulses at PC is constant, the timing of the PC dilation pulse is adjusted accurately by the delay circuit to synchronize the PC dilation pulse with the photoelectron pulses. A good synchronization position is acquired by a large number of experiments, which is approximately 235 ps relative to the starting time of the PC dilation pulse. The PC voltage at this synchronization position is about -2.5 kV. When the synchronization position is 235 ps and the photoelectron pulses are dilated, the measured gated image for the camera with pulse-dilation is shown in Fig. 8(c). Lineouts of the results from Fig. 8(c) are shown in the blue part of Fig. 8(d), which shows that the temporal resolution T of the pulse-dilation framing camera is approximately 10 ps. The temporal magnification factor M could be acquired from the PC voltage, the temporal resolution T_{MCP} of MCP imager, and the temporal resolution T of pulse-dilation framing camera. The measured M is 10 , which agrees well with the theoretical result of 10.2 calculated from equation (6).

IV. X-RAY DIAGNOSIS APPLICATIONS

The pulse-dilation framing camera is used to detect X-rays generated by a terawatt laser target device. The experimental setup of the X-ray pulse's measurement is similar to the temporal resolution measurement setup in Fig. 7(a). The difference is that the fiber bundle is not used in the X-ray measurement. Two laser pulses with wavelengths of 390 and 780 nm and pulse widths of 100 fs are emitted from the terawatt laser system. The laser with 780 nm in wavelength has an energy of 650 mJ. It is reflected by several total reflection mirrors firstly, and then irradiates a planar iron target to produce X-rays. The camera is placed outside the target chamber, and a 71 cm distance is measured between PC and iron target. As no component is placed between PC and iron target, the X-rays can reach PC freely to produce

photoelectrons. The laser with 390 nm in wavelength is reflected from another total reflector to a PIN diode, which produces a trigger signal for the pulse generator. The framing camera is working in pulse-dilation dynamic mode. A DG535 delay generator is used to adjust the trigger time precisely to synchronize the X-rays with the PC dilation pulse. Then, the gated images with pulse-dilation are obtained.

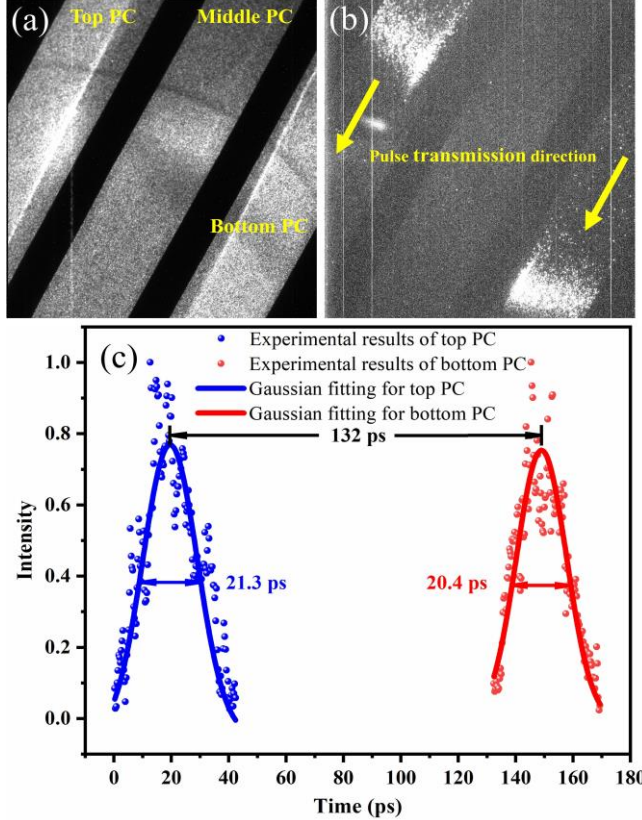


Fig. 9. (a) Static image, while the PC receives a -3 kV static DC voltage and the MCP receives a -700 V. (b) Gating image with pulse-dilation, when a DC bias of -3 kV and a dilation pulse are applied on PC, and MCP are applied with a gating pulse and a -483 V DC bias. (c) The intensity versus time distribution along the top PC and the bottom PC.

In this experiment, the middle transmission PC is used as a monitor, and it is not applied with DC voltage or dilation pulse. Firstly, the static image of the transmission PC is measured, while the PC is applied with a -3 kV static DC voltage and the MCP is biased with a -700 V. The measured image is shown in Fig. 9(a). Because that the X-rays have a nonuniform spatial distribution, there is a nonuniform intensity distribution in Fig. 9(a). Then, the gating image of the transmission PC for the camera with pulse-dilation is obtained, as shown in Fig. 9(b), which is acquired when each of the top and bottom PC is given a dilation pulse in addition to the -3 kV DC bias and the MCP is given a -483 V DC bias in addition to the gating pulse. Two coaxial cables with different lengths are used to achieve two dilation pulses reaching the top and bottom PCs at different times, which can acquire the X-rays with various times for the two PCs. The dilation pulses on the two PCs are both synchronized with the

X-ray pulses. Therefore, two gating images are obtained. The intensity distribution along MCP could be obtained from Fig. 9(b). Because of the 1:1 magnification ratio, the PC area related to the gating image is the same as that in MCP. The dilation pulse transmits across PC from left to right at a velocity of about 1.87×10^8 m/s, which was measured by the time domain reflection method [36,37]. Then, the intensity with varying transmission time along PC for the gating image was obtained from the gating image spatial distribution and the PC dilation pulse velocity, as shown in Fig. 9(c). The final results in Fig. 9(c) are calibrated by the static results in Fig. 9(a). Fig. 9(c) shows the intensity versus temporal distribution related to the X-ray pulse. The solid points and the lines represent the experimental results and the Gaussian fitting curves, respectively. The blue part is the results of the top PC, the red part is for bottom PC. The FWHMs of the Gaussian fitting curves are 21.3 ps and 20.4 ps, respectively. The two FWHMs are almost the same, and the difference is within 5%. Each Gaussian fitting curve is the convolution result of the camera's intensity versus time curve with the X-ray's intensity versus temporal distribution. Considering the FWHM of the camera's intensity versus time curve is 10 ps, the FWHM of the temporal distribution of X-ray is about 18 ps from the deconvolution result. It shows that the X-ray pulse has a width of about 18 ps. Furthermore, Fig. 9(c) also shows that, the delay time between the dilation pulses for the top and bottom PCs is about 132 ps.

V. CONCLUSION

An ultrafast pulse-dilation framing camera with combined magnetic lenses is developed. The camera uses pulsed PC to achieve a high temporal resolution, and four magnetic lenses to improve the spatial resolution. A temporal resolution of 10 ps and spatial resolution of $100\text{ }\mu\text{m}$ are obtained. The spatial resolution characteristics of the camera are studied. Different numbers of magnetic lenses are respectively applied to the camera to compare the spatial resolution characteristics. Both of the theoretical and experimental results show that the spatial resolution of the camera using single magnetic lens is the worst, and an improved spatial resolution will be obtained when the camera is applied with combined magnetic lenses. The four magnetic lenses camera has better spatial resolution than other cameras. Furthermore, the field curvatures of the camera with different number of lenses are measured. The results also show that the four magnetic lens camera has lower field curvature than other cameras, so that it has better spatial resolution and larger working area. Moreover, the axial location of the imaging plane will influence the spatial resolution uniformity for the on-axis and off-axis area, which will limit the working area. An appropriate imaging plane is obtained for the camera with four magnetic lenses, and the working area with 53 mm in diameter is achieved. The camera is used to detect X-rays, and the diagnostic results show that the width of the X-ray pulse is about 18 ps.

- [1] O. A. Hurricane, D. A. Callahan, D. T. Casey et al., Fuel gain exceeding unity in an inertially confined fusion implosion. *Nature* **506**, 343–348 (2014). doi: 10.1038/nature13008
- [2] J. G. Zhu, H. Y. Lu, Y. Zhao, et al., Study of achromatic beamline design for laser-driven femtosecond electron beams. *Nucl. Tech.* **46**, 020201 (2023) doi: 10.11889/j.0253-3219.2023.hjs.46.020201. (in Chinese).
- [3] S. R. Nagel, H. Chen, J. Park, et al., Two-dimensional time-resolved ultra-high speed imaging of K-alpha emission from short-pulse-laser interactions to observe electron recirculation. *Appl. Phys. Lett.* **110**, 14, 144102 (2017). doi: 10.1063/1.4979802
- [4] Y. Zhang, L. X. Liu, H. W. Wang, et al., Primary yields of protons measured using CR-39 in laser-induced deuteron-deuteron fusion reactions. *Nucl. Sci. Tech.* **31**, 6, 62 (2020). doi: 10.1007/s41365-020-00769-8
- [5] J. Guo, W. L. Cai, Y. S. Geng, et al., Design of the neutron slit package for Femi chopper prototype of CSNS. *Nucl. Tech.* **44**, 050201 (2021). doi: 10.11889/j.0253-3219.2021.hjs.44.050201. (in Chinese).
- [6] Y. M. Fang, X. Y. Xu, J. S. Tian, et al., Design of a control system with high stability for a streak camera using isolated ADC. *Nucl. Sci. Tech.* **29**, 2, 22 (2018). doi: 10.1007/s41365-018-0361-9
- [7] L. Yang, H. R. Cao, J. L. Zhao et al., Development of a wide-range and fast-response digitizing pulse signal acquisition and processing system for neutron flux monitoring on EAST. *Nucl. Sci. Tech.* **33**, 3, 35 (2022). doi: 10.1007/s41365-022-01016-y
- [8] P. Hu, Z. G. Ma, K. Zhao, et al., Development of gated fiber detectors for laser-induced strong electromagnetic pulse environments. *Nucl. Sci. Tech.* **32**, 6, 58 (2021). doi: 10.1007/s41365-021-00898-8
- [9] D. K. Bradley, P. M. Bell, J. D. Kilkenny, et al., High-speed gated x-ray imaging for ICF target experiments. *Rev. Sci. Instrum* **63**, 10, 4813–4817 (1992). doi: 10.1063/1.1143571
- [10] J. Y. Liu, L. H. Niu, W. D. Peng, et al., Application of a fast electrical pulse in gated multichannel plate camera. *Rev. Sci. Instrum* **78**, 5, 055104 (2007). doi: 10.1063/1.2737750
- [11] D. K. Bradley, P. M. Bell, O. L. Landen, et al., Development and characterization of a pair of 30–40 ps x-ray framing cameras. *Rev. Sci. Instrum* **66**, 1, 716–718 (1995). doi: 10.1063/1.1146268
- [12] M. Koga, H. Shiraga. Gain depletion of X-ray framing camera. *Rev. Sci. Instrum* **88**, 083514, (2017). doi: 10.1063/1.4999757
- [13] J. D. Kilkenny. High speed proximity focused X-ray cameras. laser part, *Beams* **9**, 1, 49–69 (1991). doi: 10.1017/S0263034600002330
- [14] P. M. Bell, J. D. Kilkenny, R. L. Hanks, et al., Measurements with a 35 psec gate time microchannel plate camera. *Proc. SPIE* **1346**, 456–464 (1991). doi: 10.1117/12.23371
- [15] J. H. Liu, Z. Ge, Q. Wang et al., Electrostatic-lenses position sensitive TOF MCP detector for beam diagnostics and new scheme for mass measurements at HIAF. *Nucl. Sci. Tech.* **30**, 10, 152 (2019). doi: 10.1007/s41365-019-0676-1
- [16] S. T. Ivancic, W. Theobald, K. Churnetski, et al., Design of the high-yield time-gated x-ray hot-spot imager for OMEGA. *Rev. Sci. Instrum* **93**, 11, 113521 (2022). doi: 10.1063/5.0101673
- [17] J. Y. Liu, J. Wang, B. Shan, et al., An accumulative x-ray streak camera with sub-600-fs temporal resolution and 50-fs timing jitter. *Appl. Phys. Lett.* **82**, 20, 3553–3555 (2003). doi: 10.1063/1.1577213
- [18] J. L. Kline, S. H. Batha, L. R. Benedetti, et al., Progress of indirect drive inertial confinement fusion in the United States. *Nucl. Fusion* **59**, 11, 112018 (2019). doi: 10.1088/1741-4326/ab1ecf
- [19] K. Engelhorn, T. J. Hilsabeck, J. Kilkenny, et al., Sub-nanosecond single line-of-sight (SLOS) x-ray imagers. *Rev. Sci. Instrum* **89**, 10, 10G123 (2018). doi: 10.1063/1.5039648
- [20] H. Z. Cai, Q. Y. Luo, K. X. Lin, et al., Development of an ultrafast detector and demonstration of its oscilloscopic application. *Nucl. Sci. Tech.* **33**, 6, 72 (2022). doi: 10.1007/s41365-022-01055-5
- [21] T. J. Hilsabeck, J. D. Hares, J. D. Kilkenny, et al., Pulse-dilation enhanced gated optical imager with 5 ps resolution. *Rev. Sci. Instrum* **81**, 10, 10E317 (2010). doi: 10.1063/1.3479111
- [22] S. R. Nagel, T. J. Hilsabeck, P. M. Bell, et al., Investigating high speed phenomena in laser plasma interactions using dilation x-ray imager. *Rev. Sci. Instrum* **85**, 11, 11E504 (2014). doi: 10.1063/1.4890396
- [23] C. Trosseille, S. R. Nagel, and T. J. Hilsabeck, Electron pulse-dilation diagnostic instruments. *Rev. Sci. Instrum* **94**, 2, 021102 (2023). doi: 10.1063/5.0128802
- [24] S. R. Nagel, T. J. Hilsabeck, P. M. Bell, et al., Dilation x-ray imager a new/faster gated x-ray imager for the NIF. *Rev. Sci. Instrum* **83**, 10, 10E116 (2012). doi: 10.1063/1.4732849
- [25] H. Z. Cai, W. Y. Fu, Y. L. Bai, et al., Simulation of a dilation x-ray framing camera. *J. Electron. Imag* **26**, 4, 043003 (2017). doi: 10.1117/1.JEI.26.4.043003
- [26] S. R. Nagel, A. C. Carpenter, J. Park, et al., The dilation aided single-line-of-sight x-ray camera for the National Ignition Facility: Characterization and fielding. *Rev. Sci. Instrum* **89**, 10, 10G125 (2018). doi: 10.1063/1.5038671
- [27] C. Trosseille, A. M. Garafalo, M. S. Dayton, et al., Characterization of the hardened single line of sight camera at the National Ignition Facility. *Rev. Sci. Instrum* **93**, 8, 083516 (2022). doi: 10.1063/5.0100981
- [28] H. Z. Cai, X. Zhao, J. Y. Liu, et al., Dilation framing camera with 4 ps resolution. *APL Photonics* **1**, 1, 016101 (2016). doi: 10.1063/1.4945350
- [29] J. Feng, K. Engelhorn, B. I. Cho, et al., A grazing incidence x-ray streak camera for ultrafast, single-shot measurements. *Appl. Phys. Lett.* **96**, 13, 134102 (2010). doi: 10.1063/1.3371810
- [30] I. Konvalina, I. Müllerová, Properties of the cathode lens combined with a focusing magnetic/immersion-magnetic lens. *Nucl. Instrum. Methods Phys. Res. Sect. A* **645**, 1, 55–59 (2011). doi: 10.1016/j.nima.2010.12.232
- [31] Z. Chang, A. Rundquist, J. Zhou, et al., Demonstration of a sub-picosecond x-ray streak camera. *Appl. Phys. Lett.* **69**, 1, 133–135 (1996). doi: 10.1063/1.118099
- [32] M. M. Shakya and Z. H. Chang. Achieving 280 fs resolution with a streak camera by reducing the deflection dispersion. *Appl. Phys. Lett.* **87**, 4, 041103(2005). doi: 10.1063/1.2001732
- [33] H. Z. Cai, W. Y. Fu, D. Wang, et al., Dilation x-ray framing camera and its temporal resolution uniformity. *Optics Express* **27**, 3, 2817–2827 (2019). doi: 10.1364/OE.27.002817
- [34] H. Z. Cai, W. Y. Fu, D. Wang, et al., Large-format pulse-dilation framing tube with 5 lp/mm spatial resolution. *Optik* **185**, 441–446 (2019). doi: 10.1016/j.jleo.2019.03.105
- [35] A. G. MacPhee, A. K. L. Dymoke-Bradshaw, J. D. Hares, et al., Improving the off-axis spatial resolution and dynamic

-
- range of the NIF X-ray streak cameras. *Rev. Sci. Instrum.* **87**, 11, 11E202 (2016). doi: 10.1063/1.4960376
- [36] H. Z. Cai, W. Y. Fu, D. Wang, et al., Synchronous gating in dilation x-ray detector without 1:1 image ratio. *Optics Express* **27**, 9, 12470–12482 (2019). doi: 10.1364/OE.27.012480
- [37] Z. H. Chang, B. Shan, X. Q. Liu, et al., Gated MCP framing camera with 60 ps exposure time. *Proc. SPIE* **2549**, 53–59, (1995). doi: 10.1117/12.218320